IEEE Access
Multidisciplinary | Rapid Review | Open Access Journal

Received February 8, 2019, accepted May 1, 2019, date of publication May 9, 2019, date of current version May 22, 2019.

Digital Object Identifier 10.1109/ACCESS.2019.2915786

A 3D Iris Scanner From Multiple 2D Visible Light Images

DANIEL P. BENALCAZAR[1], (Member, IEEE), DIEGO BASTIAS[1], CLAUDIO A. PEREZ[1], (Senior Member, IEEE), AND KEVIN W. BOWYER[2], (Fellow, IEEE)

[1]Department of Electrical Engineering and Advanced Mining Technology Center, Universidad de Chile, Santiago 8370451, Chile
[2]Department of Computer Science and Engineering, University of Notre Dame, Notre Dame, IN 46556, USA

Corresponding author: Claudio A. Perez (clperez@ing.uchile.cl)

This work was supported by the Comisión Nacional de Investigación Científica y Tecnológica (CONYCYT) through the Fondo Nacional de Desarrollo Científico y Tecnológico (FONDECYT) under Grant 1161034 and by the Department of Electrical Engineering, Universidad de Chile.

ABSTRACT The development of new methods for biometrics using the 3-D surface of the iris could be useful in various applications, such as reliable identity verification of people, when only segments of the iris are available, the study of how the iris code changes with pupil dilation, and studying acute angle glaucoma and its relation to the 3-D iris structure. The goal of this paper was to build a 3-D model of the iris surface from several 2-D iris images, adding depth information to the iris model. We developed a 3-D iris scanner, which reconstructs a 3-D mesh model of the iris surface from several 2-D visible light images. First, a smartphone camera captures visible light iris images from different angles in a controlled illumination environment. Then, a structure-from-motion algorithm reconstructs a point-cloud 3-D model. Finally, the best-fitting 3-D mesh model is obtained using the screened Poisson surface reconstruction technique. Our results include the reconstruction of the 3-D iris models of ten subjects. These models contain an average of 11,000 3-D points. The spatial resolution of our device was measured as 11 μm by scanning a 3-D pattern of known dimensions. The 3-D model of the iris is compared with the results from an optical coherence tomography (OCT) performed on one iris. Our results show that our new 3-D iris scanning method produces a model with potential applications in biometrics and ophthalmology.

INDEX TERMS 3D iris reconstruction, 3D iris scanner, biometrics, iris recognition, structure from motion.

I. INTRODUCTION

The need for accurate identity verification systems has driven the research on iris recognition techniques. These techniques exploit the texture of the human iris because it exhibits a distinctive pattern with great variability among individuals [1], [2]. Iris recognition is currently the most reliable biometric technology on the market because of its non-invasive, accurate, and robust methodology [3], [4]. Furthermore, iris recognition has succeeded in both small- and large-scale applications. Some large-scale uses include United Arab Emirates border-crossing [5] and India's Unique ID program [6]. Iris recognition was also used to create a voter registration list in Somaliland [7].

One of the main reasons for the success of iris recognition technology is its high accuracy. Daugman demonstrated that a false match rate of 1 in 4 million could be achieved when using a fractional Hamming Distance (HD) of 0.33 [1]–[8]. The variability in iris texture as analyzed by Daugman's method is as great for left and right eyes of the same person, and between identical twins, as it is for irises of unrelated persons [1]–[9]. By contrast, the variability in fingerprint analysis would produce inadmissible false matches in large databases [2], which is why India, for example, uses iris recognition as well as fingerprints for its Unique ID program [6].

Although iris recognition is a well-developed technique with successful applications, there are still areas for improvements. First, iris recognition could encounter the same issue as fingerprint analysis if the database were large enough. For instance, in a database of one billion individuals, a false match rate of 1 in 4 million indicates that 250 people have similar iris codes. In addition, it is normal to have partial occlusions of the iris due to eyelashes, eyelids, and specular reflections.

The associate editor coordinating the review of this manuscript and approving it for publication was Shubhajit Roy Chowdhury.

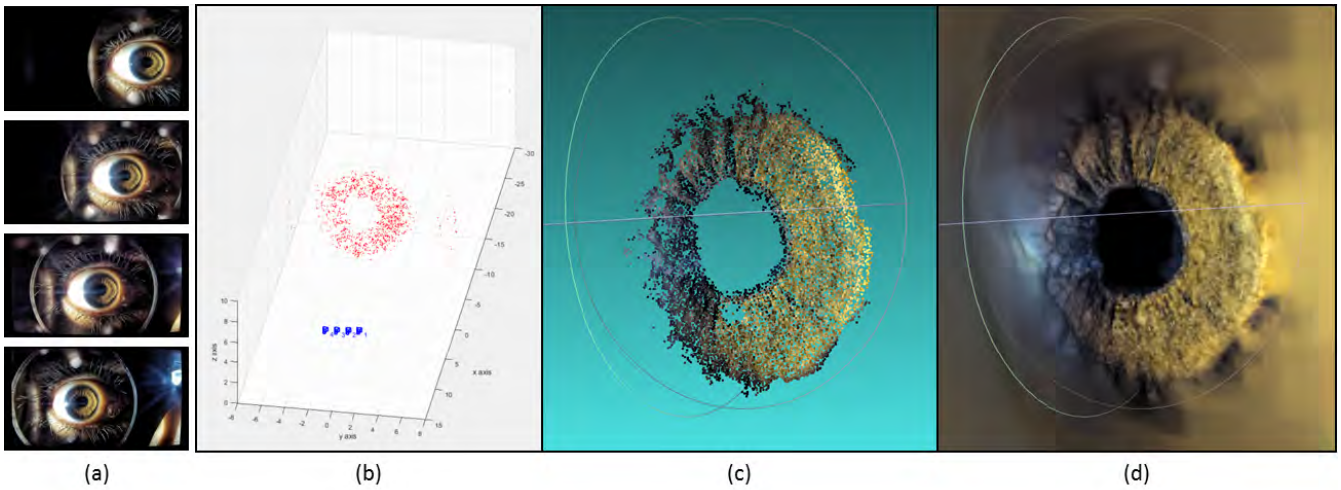

FIGURE 1. Process of 3D Iris Reconstruction. (a) Image acquisition from different views. (b) Camera pose estimation (blue) and sparse 3D reconstruction (red). (c) Dense 3D point-cloud reconstruction. (d) Mesh surface reconstruction.

When there is less iris available for matching, the accuracy that can be achieved is lower. Moreover, iris recognition techniques assume that the iris is flat, when, in fact, it is a three-dimensional organic structure. The human iris dilates and contracts using two muscle systems, a sphincter and several radial dilator muscles, in order to control the amount of light that hits the retina [10]. These muscle systems cause the surface of the iris to have a 3D relief that can be visualized in Optic Coherence Tomography (OCT) [11]. However, when this complex 3D structure is mapped onto a 2D plane, all depth information is lost. Recapturing depth information could, in principle, enhance the amount of information we can extract from the iris. Our 3D scanner allows studying, in detail, the impact of pupil dilation on Daugman's rubber sheet model of iris surface deformation. The results of this research will allow us to measure the displacement of the iris structure as a function of the pupil dilation in 3D, and to relate the iris displacements to the rubber sheet model used for identification. This, in turn, could lead to the formulation of more accurate models for iris normalization, even with extreme dilation differences [12].

Previous work in this area includes the following. Bastias *et al.* [13] reconstructed a 3D model of the iris from several NIR images in order to capture the depth information of the iris surface. A raspberry-pi V2 camera was used to capture NIR iris images along a circular arch [13]. Then, a photogrammetry algorithm was used to reconstruct a 3D model, thus creating a new method for human iris analysis [13]. Issues with that method include the noisy nature of the camera, the resolution, and the plane correction needed to integrate all the images [13]. In recent work, Benalcazar *et al.* [14] used lateral visible-light (VL) illumination to capture highly textured images of the iris at a resolution of 16Mpx. Lateral illumination allowed VL images to capture structural details of the iris [14]. In fact, a combination of lateral and frontal illumination showed slightly superior iris-recognition performance than that of frontal NIR illumination [14]. Our work builds upon these previous studies to create a robust and reliable method of 3D iris scanning that is not only useful for biometrics, but also is promising as a less expensive screening tool for Acute Angle Glaucoma, a disease currently diagnosed with an OCT [13]–[15].

The proposed 3D iris scanning methodology consists of four main stages, as is illustrated in Fig. 1. First, VL images of the iris are captured from different perspectives, as shown in Fig.1a. Then, we use Structure from Motion (SfM) [16] to jointly estimate the camera pose of every image and a sparse 3D model of the iris. Our method applies several constraints to adapt the SfM algorithm specifically for the iris. Fig.1b shows camera positions in blue, and the initial point-cloud model of the iris in red. Then, a dense 3D reconstruction is performed by extracting more keypoints from each image, as shown in Fig.1c. Finally, the point-cloud model is converted into a mesh surface by the Screen Poisson Surface Reconstruction technique [17]. This method produces a mesh representation of the iris surface that integrates the depth information of a large number of points on the iris. Fig.1d shows the details that are captured from the iris in the final mesh representation. With the additional depth information, extra degrees of freedom can allow iris recognition to be applied in even larger databases than is currently possible, thus extending the scope of iris recognition.

The following are the main contributions of this study. First, we improve the scanning device so that iris images have better resolution, less noise, and additional color information. Second, we improve the preprocessing stage by adding lens-distortion correction [18], [19] and local Laplacian contrast enhancement [20]. Third, we adapt the SfM pipeline for this specific application to make the system more robust and less computationally expensive. Fourth, we reconstructed 3D iris models for 10 subjects. Fifth, we evaluate the performance of our 3D iris scanner in terms of spatial resolution by

scanning objects of known dimension depths. Sixth, we compared our 3D reconstruction with the OCT of one iris. The OCT is a paid medical exam, and therefore, it was performed for just one volunteer to provide a qualitative comparison with our method, to show the promise of our approach as an alternative to OCT.

II. REVIEW ON 3D RECONSTRUCTION

Methods to produce a detailed reconstruction of objects or scenes from images and video have improved significantly over time [21]. Application of these technologies varies from object scanning to robotic vision and city mapping. New algorithms, as well as increasing CPU and GPU power, allow processing thousands of images in a linear-time incremental manner [16]. For example, a collection of internet images has been used to reconstruct buildings and even city blocks [22]. Other research has focused on real time implementations for environment mapping and robotic navigation [23], [24]. In this section, we present a brief survey of 3D reconstruction methodologies that have inspired our pipeline.

Methods for 3D representation of the environment from digital images can be grouped into two areas [21]. Both obtain 3D points from keypoints in images from various perspectives. Thus these methods need several highly textured images to produce an optimal reconstruction [21], [25]. The first group is Visual Simultaneous Localization and Mapping (SLAM), which processes image frames, from video or real time, one by one [23], [26]. This method aims to reduce the uncertainty of the measurements with each new observation, and incorporates new 3D points into the model from each image [23], [24], [26]. The second group, Multi-View Stereo (MVS), processes the unsorted images in a batch [16], [27]. MVS treats 3D reconstruction as an optimization problem: given a group of images, find the camera poses and 3D model that minimize the total re-projection error [21]. The re-projection error is the distance between a keypoint and the pixel where the associated 3D point is projected back onto the image plane [21].

Visual SLAM was conceived as a method for autonomous robotic navigation without the need for sophisticated sensors such as LIDAR [23], [24], [26]. This method utilizes a Kalman filter to jointly estimate the camera trajectory and the position of landmarks in the environment [23], [26]. Visual Slam is an active area of research where state-of-the-art implementations can run in real time. For instance, the ORB-SLAM system utilizes ORB features, which are fast and robust, to generate a map of the environment for robotic navigation [24]. ORB-SLAM has a robust mechanism that stores only important frames, manages automatic model initialization, and detects traversing on the same path for loop closing [24]. Fang *et al.* [28] also implemented Visual SLAM with ORB features, but with an FPGA architecture to reduce power consumption. The PL-SLAM system extracts point and line features to work even with low textured images [29]. The Visual SLAM paradigm can also be used for augmented reality systems in real time [30].

MVS estimates all the camera poses and an initial sparse 3D model using a process known as Structure from Motion (SfM) [21], [22]. SfM uses epipolar geometry to find the relative spatial motion, in terms of the Essential Matrix, between two cameras observing the same scene [16]. The Essential Matrix represents the transformation (rotation and translation) of coordinate systems from one camera to the next [25]. If one camera is fixed, the absolute position and orientation of the other cameras can be found [25], [31]. After finding all camera poses, the coordinates of the 3D points in the model are triangulated [14], [25]. SfM has a final refinement step which is called Bundle Adjustment [32]. This is the step where the camera poses and 3D model points are jointly optimized to minimize the re-projection error. The re-projection error can be lowered even to sub-pixel values in this step [21].

MVS builds upon the output of the SfM process to obtain a more detailed model [27]. This model is called a dense reconstruction, and can be represented in different formats: point-cloud [16], [27], depth-map [33], voxel [34], and deformable polygonal mesh [35]. Furukawa et al. proposed a versatile point-cloud representation, in which each 3D point is represented by a small rectangular oriented plane [27]. This MVS implementation is based on a repeated process of match, expand, and filter [27]. This process incorporates new patches, expands them filling uncharacterized areas, and then trims the patches that result in a faulty geometry [27]. At the end, this implementation is capable of finding detail even in low texture regions from non-keypoint pixels [27]. The best known implementation of MVS and SfM is that of Agarwal et al.: ''Building Rome in a day'' [22]. They utilized 150,000 assorted images of Rome from the internet, and produced a point-cloud model of the city, which includes the most famous buildings [22]. Melow et al. improved the MVS algorithm by identifying and removing shading and reflectance from the model [36]. Lim et al. adapted the MVS paradigm to scan the digestive system of human beings [37]. Their endoscope system proves that MVS can work in biomedical applications [37].

III. METHODS

A. IRIS IMAGING DEVICE

The first step towards reconstructing a 3D model of the iris is capturing sharp well-illuminated images of the iris from different viewpoints. These images need to have high texture and high resolution in order to obtain as many keypoints as possible. Additionally, as we observed in our previous research [13], those images need to have a consistent pupil dilation level; thus, a controlled illumination environment is also needed. Finally, all the components of the device have to be mounted on an ergonomic structure that minimizes motion related artifacts. With all of these considerations in mind, the proposed image acquisition device consists of the following components: a cellphone camera, a rail on which the cellphone moves freely in front of the iris, an LED illumination setup, an illumination control circuit, and a frame

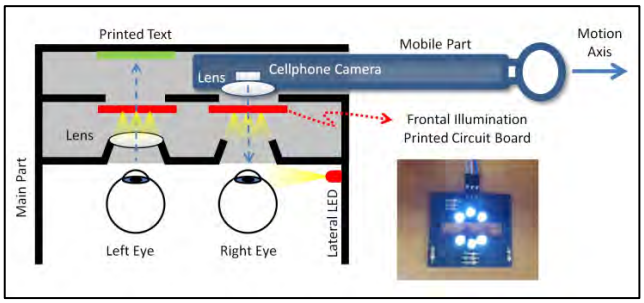

FIGURE 2. Top view of the device schematics and a picture of the frontal illumination PCB. The left half of the device allows the users to focus their gaze on printed letters, while the right side allows the camera to capture close range images of the right eye in a controlled illumination environment. The cellphone camera moves in a linear trajectory while taking pictures of the right eye from different viewpoints (angles).

FIGURE 3. Picture of the image acquisition device.

on which all these components are mounted. Fig. 2 shows the device schematics. The device was inspired by the designs of Bastias *et al.* [13] and Mariakakis *et al.* [38], and presents slight improvements on the one presented in [14].

The frame consists of two parts: a main part and a mobile part. The main part is a chamber based on Google Cardboard VR glasses [39]. This chamber produces a steady structure to capture images of the eye while blocking external light sources. The structure was laser-cut in acrylic for stability and painted opaque black to reduce specular highlights [14]. The illumination setup and circuitry are allocated to this structure. The mobile part holds the camera and a close-range lens. This part was 3D printed and also painted opaque black. The 3D-printed piece includes a handle and a rail that allows the two parts to move freely along the axis shown in Fig. 2. The subject remains fixed with respect to the main part; thus, when the mobile part moves along the axis, the camera can take several pictures of the right eye from different perspectives. Fig. 3 shows a picture of both parts of the device.

Image acquisition is done with a Samsung S6 cellphone with a macro lens. This macro lens is a biconvex lens, 25mm diameter and focal distance of 45mm. It captures 16Mpx VL images at 4 cm from the iris [14]. The eye is illuminated with white LEDs from the front and from the side. The lateral LED enhances the contrast in the images since it produces shadows from the relief on the surface of the iris [14]. The frontal LEDs maintain uniform illumination across the iris and the sclera [14]. The frontal illumination PCB was based on the design in [13]. This PCB allows the illumination to be fixed while the camera moves behind it. The device was designed so that the specular reflections from the frontal LEDs fall on the pupil region, avoiding interference with the iris texture. Another feature included to reduce eye motion is a printed text of the first seven letters of the alphabet, as is shown schematically in Fig. 2. This helps to fix the gaze of the subject's left eye, by the operator asking the subject to focus their attention on a specific letter. Also, to avoid variations in pupil dilation, the left eye is illuminated with a duplicate of the frontal illumination PCB. This helps in maintaining constant pupil dilation between frames because both eyes receive the same amount of light. Light intensity of both circuits, as well as that of the lateral LED, is controlled independently using pulse width modulation. The illumination controller is the white box on top of the device shown in Fig. 3.

B. IMAGE PROCESSING

1) LENS DISTORTION CORRECTION

As is usual in the first step of an image processing pipeline, it was necessary to correct the lens distortion between the cellphone camera and the macro lens to improve the image processing results, reduce the complexity of the camera model, and the processing time [21]. To estimate both lens distortion coefficients and the camera model, we used the Matlab implementation [40] of the camera calibration process [18], [19]. This process uses a set of between 10 and 20 images of a checkerboard pattern in different locations of the image [40]. The pattern is placed at the same distance from the camera as that of the iris. With the location of the corners in the checkerboard images, this algorithm computes the intrinsic parameters of the camera model such as: focal length, principal point, skew, radial distortion, and tangential distortion. With this information, lens distortion correction is performed on the iris images.

The camera model is the mathematical transformation that represents the way in which 3D points of the real world are projected onto the pixels of the image. Equation 1 describes the pin-hole camera projection model [21], [24]:

$$\tilde{p} = \begin{bmatrix} f_x & s & c_x \\ 0 & f_y & c_y \\ 0 & 0 & 1 \end{bmatrix} \times \begin{bmatrix} r_{11} & r_{12} & r_{13} & t_x \\ r_{21} & r_{22} & r_{23} & t_y \\ r_{31} & r_{32} & r_{33} & t_z \end{bmatrix}^{-1} \times P, \tag{1}$$

$$\tilde{p} = K \times T^{-1} \times P, \tag{2}$$

where P is a 3D world point $\tilde{P}$, is the coordinates of the pixel in which P is projected in homogeneous coordinates, f_x and f_y are the horizontal and vertical focal lengths in pixels, s is the skew, (c_x, c_y) are the coordinates of the principal point which is the intersection of the optical axis with the image plane, r_{ij} are rotation coefficients of the camera pose, and

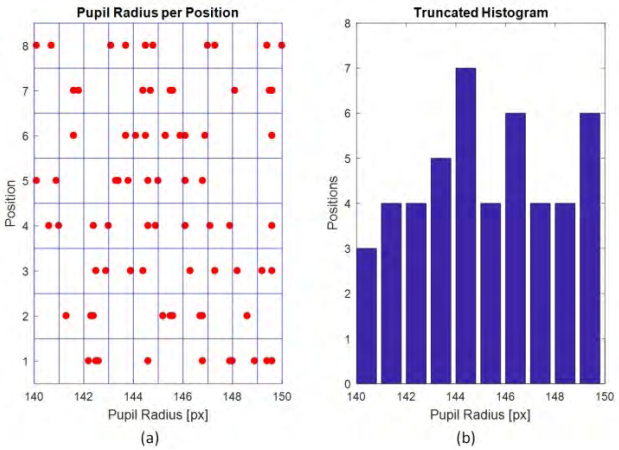

FIGURE 4. Pupil dilation in an image set. (a) Pupil radius of 10 burst images from 8 camera positions. (b) Histogram of positions available per pupil radius. A radius of 144.5 pixels was present at 7 different camera positions; those images were therefore selected to reconstruct the 3D model.

the vector (t_x, t_y, t_z) is the translation of the camera position from the origin of the 3D world coordinates. K is the intrinsic matrix, which is the result of the camera calibration process. Finally, T is the extrinsic matrix, which is computed in later steps.

2) DILATION-BASED IMAGE SELECTION

SfM and MVS methods assume that the scanned object does not deform between frames. However, the human iris changes because of dilation, which is a form of distortion [10]. The greater the variation in iris dilation in the images used in the 3D reconstruction process, the greater the noise level in the results. Illuminating both eyes with the same amount of light improves the stability in the dilation; however, small dilation changes naturally still occur. To further reduce dilation related problems, we propose an image selection method that identifies a set of images with the same dilation to generate a 3D model. First, we take a burst of 10 or more images of the eye at each camera position. Then, we identify the pupil in each image and measure its radius. Finally, we compute a histogram of the number of positions available per pupil radius. The dilation level which is present in the greatest number of positions is then chosen, and all the images that form that histogram bin are used in the reconstruction of the 3D model. Fig.4 illustrates the amount of dilation present in a typical image set, and the image selection method. At the end of this step, a group of images having small dilation variation, and coming from the largest number of camera positions available, is selected.

3) IRIS SEGMENTATION

We segmented the iris in the selected images by masking out the pupil, the sclera, eyelids and eyelashes [8], [41]. Although the 3D model can be reconstructed without iris segmentation, this process removes irrelevant 3D points from eyelids and eyelashes in the final 3D model.

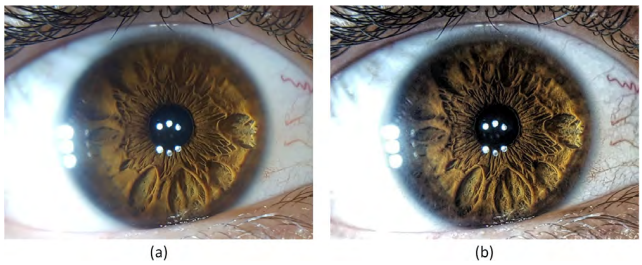

FIGURE 5. Contrast Enhancement of iris images by means of Local Laplacian [20]. (a) Original Image. (b) Enhanced Image.

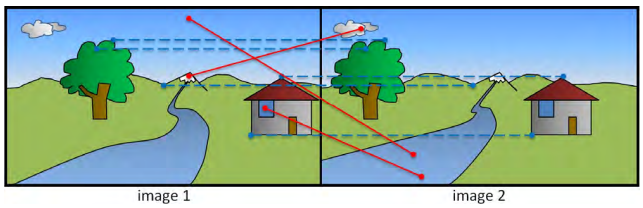

FIGURE 6. Slope-based match filter. The two images are placed side by side horizontally and line segments join the matched keypoints. Since the camera moves on the X axis, line segments are expected to have a slope of 0 (blue lines). However, mismatched keypoints have similar descriptors, but produce slopes different from 0 (red lines).

4) CONTRAST ENHANCEMENT

The final preprocessing step is to enhance the dynamic range of brightness in the iris region. This step improves the number of keypoints that can be extracted from the iris. A Local Laplacian filter was used for contrast enhancement [20]. This filter uses information of only local patches and, thus, eliminating extreme bright and/or extreme dark zones is not required. Fig. 5 shows the results of this stage.

C. KEYPOINT EXTRACTION AND MATCHING

1) KEYPOINTS AND DESCRIPTORS

The starting step in SfM to produce the 3D model is identifying distinctive features across all the images. The coordinates of those features help to infer the pose of the camera for each image, as well as establishing an initial sparse 3D model. The development of robust and fast feature detectors and descriptors, such as SIFT, SURF, and ORB, was a crucial factor in developing the modern SfM and MVS algorithms [21]. We use SURF key-points, as well as its 64-element descriptor, because it is efficient and invariant to lighting, scale, and rotation [25], [42], [43].

2) KEYPOINT MATCHING AND SLOPE-BASED FILTER

Keypoints of two images can be matched by finding the Euclidian distance of their descriptors. However, if the texture is similar in different regions of the object, some points can be matched incorrectly. Those mismatches diminish the precision of the essential matrix and the object reconstruction. In order to identify those outliers, we make use of the fact that the camera moves in a linear trajectory. That linear motion creates a predominant effect of iris translation on the x axis from image to image. Fig. 6 shows a graphic representation of our slope-based filter. First, for each keypoint in image 1,

we rank all the keypoints in image 2 according to the distance between their descriptors. Then, for the keypoint pair with the smallest distance, we compute the slope of the line that joins them when the two images are placed side by side horizontally. If the slope is between $\pm 5°$, the match is accepted; otherwise, the match is rejected, and the pair of points with the second best distance is tested. This process is repeated until each keypoint from image 1 is mapped with one keypoint of image 2. In this way, incorrect matches are removed.

At the end of this step, keypoints and descriptors are extracted from the images, and they are matched among consecutive images.

D. SPARSE 3D RECONSTRUCTION

1) CAMERA POSE ESTIMATION

The camera pose consists of the position and orientation of the camera in space, which can be determined from the essential matrix between two images. The essential matrix is a 3×3 matrix which encodes the Epipolar geometry that results from projecting one point in space P onto two different cameras or views to produce the corresponding points $\tilde{p}_1$ and $\tilde{p}_2$ [21], [25]. The two corresponding points from this projection are related with the essential matrix [44] given by:

$$\tilde{x}_2 \times E \times \tilde{x}_1 = 0, \tag{3}$$

where $\tilde{x}_1$ and $\tilde{x}_2$ are the normalized coordinates of the corresponding points $\tilde{p}_1$ and $\tilde{p}_2$, and E is the Essential Matrix [25], [44]. The essential matrix can be resolved with a minimum number of 8 corresponding points [44], [45]. To reduce the error caused by incorrect matches, a RANSAC process is used in the computation of the essential matrix [25], [45]. This process identifies and removes the outliers that might have passed through the previous filtering stage. The essential matrix encodes the relative camera pose for two different angles (views). If one of them is known, we can compute all the r_{ij} coefficients, as well as (t_x, t_y, t_z), in the pin-hole camera projection model in (1). In our algorithm, the pose of the first camera is fixed in advance, and the pose of the subsequent views is determined with the described method.

2) POINT-CLOUD 3D RECONSTRUCTION

Once the pose of the camera is found for each image, all the matches can be projected onto the 3D space to form a Sparse 3D reconstruction. The projection process consists of finding the 3D line that joins the center of the camera with a keypoint, and extending it. Such a 3D line is called a bundle [21]. The process is repeated for each camera position. The point in space where the bundles of corresponding keypoints meet is considered to be a 3D point in the point-cloud model. Since a keypoint can usually be tracked in more than two views, the bundles might not intersect at the same exact point. Therefore, the 3D point is the one that produces the least error in the intersection. The process is repeated for each keypoint to obtain all the 3D points in the point-cloud model.

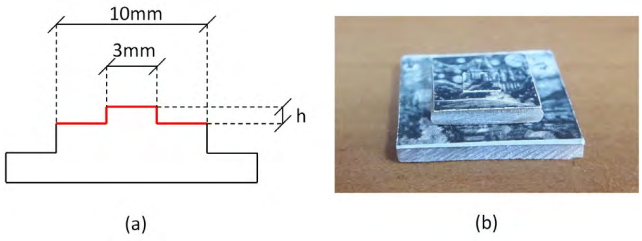

FIGURE 7. Pattern of known spatial dimensions to test 3D scanning accuracy. Only the red surfaces of the diagram were used in the analysis. Three patterns were created with final step height h of 75μm, 150μm, and 375μm.

Data of the matching points and views are managed using the track format to make the process more efficient [21]. A track j is conformed by a 3D point P_j, the camera models of all the images I on which P_j is visible, and the keypoints $\tilde{p}_{ij}$ which generated the 3D point [21].

3) BUNDLE ADJUSTMENT

A refinement process in the 3D reconstruction is called Bundle Adjustment. This process consists of jointly optimizing the camera poses and the point-cloud model to minimize the re-projection error [21], [32]. The re-projection consists of projecting the point-cloud model back to each image using the calibrated camera model (1) [21], [25]. In this sense, the error is the distance between a projected point and the keypoint that originated it. The goal is to find the camera poses and 3D points that minimize the total error given by:

$$error\,(T, P) = \sum_j \sum_{i \in V(j)} \left(\alpha_{ij} K T_i^{-1} P_j - \tilde{p}_{ij} \right)^2, \tag{4}$$

where j is the track, i is the camera view, K is the intrinsic matrix, T_i is the extrinsic matrix, P_j is a 3D point in Cartesian coordinates, α_{ij} is a constant that represents the normalization from homogeneous coordinates to Euclidean coordinates, and $\tilde{p}_{ij}$ is a keypoint.

At the end of this step, the accurate position of the camera is found for each image, as well as the initial point-cloud model of the iris tissue. On average, the reconstructed models have 2000 3D points at this step.

E. DENSE 3D RECONSTRUCTION

With the purpose of increasing the number of keypoints and 3D points, we acquired new keypoints using the minimum eigenvalue algorithm by Shi and Tomasi [46]. This technique extracted five times more keypoints than SURF from our images. Then, the 3D points were computed using the calibrated camera models of each view from the sparse reconstruction. After that, the bundle adjustment was executed a second time to refine the model. Finally, the normal to each 3D point was initialized to be perpendicular to the iris plane, and they were refined using Meshlab, an open-source software for 3D model processing [47]. At this stage, the number of 3D points in the point-cloud model is over 10,000 on average.

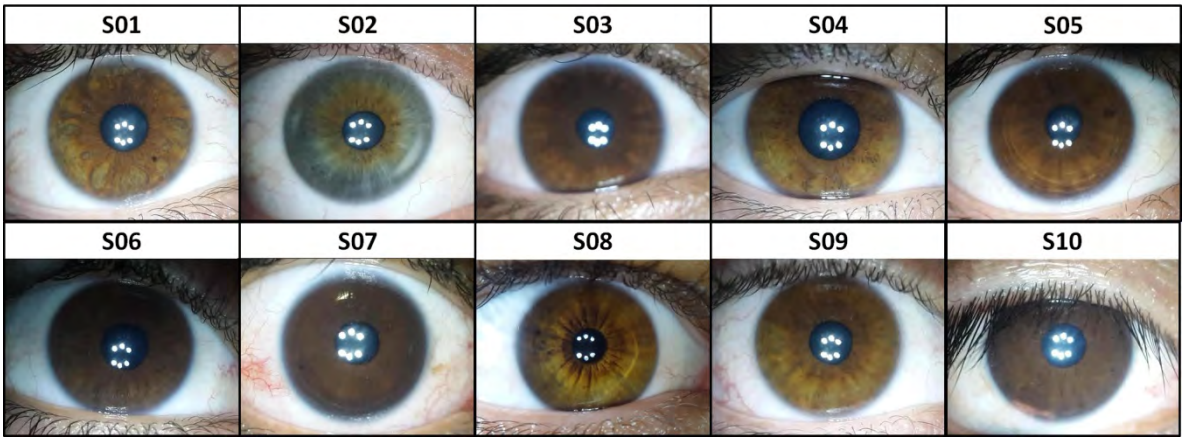

FIGURE 8. Irises captured with frontal VL for the 10 subjects included in the 3D iris model reconstruction.

The final step in our 3D reconstruction pipeline was the estimation of a mesh model for the iris. To accomplish this, we used the Meshlab implementation of the Screen Poisson Surface Reconstruction algorithm [17], [47]. This algorithm estimates the best-fitting mesh for the point cloud, and is robust to clutter [17]. This mesh helps to fill patches where the iris texture is uniform and an insufficient number of keypoints is available.

F. SCANNING RESOLUTION MEASUREMENT

After developing the 3D iris scanning methodology, it is necessary to determine the smallest spatial detail the proposed method is able to resolve. For this purpose, we scanned 3D patterns of known dimensions and analyzed the Signal to Noise Ratio (SNR). The shape of the pattern is a flat surface with a step in the middle, as is shown in red in Fig. 7. The pattern needs to have a rich texture so that our proposed methodology can be applied. That is why the flat surfaces contain a high texture picture printed on sticker paper over a rigid copper/acrylic sheet (PCB material). The height of step h is controlled by varying the number of paper layers. Each paper layer has a thickness of 75μm. In total, three patterns were created using one, two, and five layers. The patterns were scanned with the same device and same illumination settings as used for the iris.

We compute the signal to noise ratio, SNR [46], using:

$$SNR = \frac{A}{\sigma}, \tag{5}$$

where A is the amplitude of the signal and σ is the standard deviation of the noise. We take the measured value of h in the 3D model as the amplitude A.

We compared the performance of our SfM pipeline against that of two general-purpose SfM implementations available online. The first SfM software is VisualSFM [16] for the sparse reconstruction and CMVS [27] for the dense reconstruction. The second software is Regard 3D, available online on: http://www.regard3d.org/. For the test, we compared the

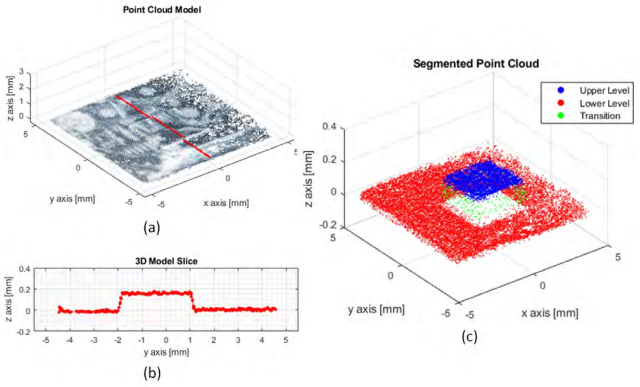

FIGURE 9. Example of the scanned 3D spatial pattern for h = 150μm. (a) Point cloud model and extracted cross section. (b) Corresponding 2D cross section. (c) Segmented point cloud.

reconstruction error in the 3D patterns of Fig. 7. Since the ground truth is the height of the step h, the reconstruction error can be computed as:

$$error = \frac{1}{N+M}\left(\sum_{i=1}^{N}|Zup_i - h| + \sum_{i=1}^{M}|Zlow_i|\right), \tag{6}$$

where Zup_i is a 3D point in the upper level, $Zlow_i$ is a point in the lower level, and N and M are the total number of points in the upper level and the lower level, respectively.

G. SUBJECTS FOR 3D IRIS RECONSTRUCTION

Using the proposed method, we scanned 10 subjects to build the 3D iris models. The subjects' irises are shown in Fig. 8 for frontal VL, and the typical iris appearances are shown for both dark and light colored eyes. Within this group, there is one green iris, three dark brown irises, and six light brown irises. We imaged their right eyes with the proposed device using a combination of lateral and frontal VL to enhance iris texture. The image acquisition time is approximately 30 s for 6 images of the iris. In the future, this time could be reduced by using an automatic scanning procedure such as controlling

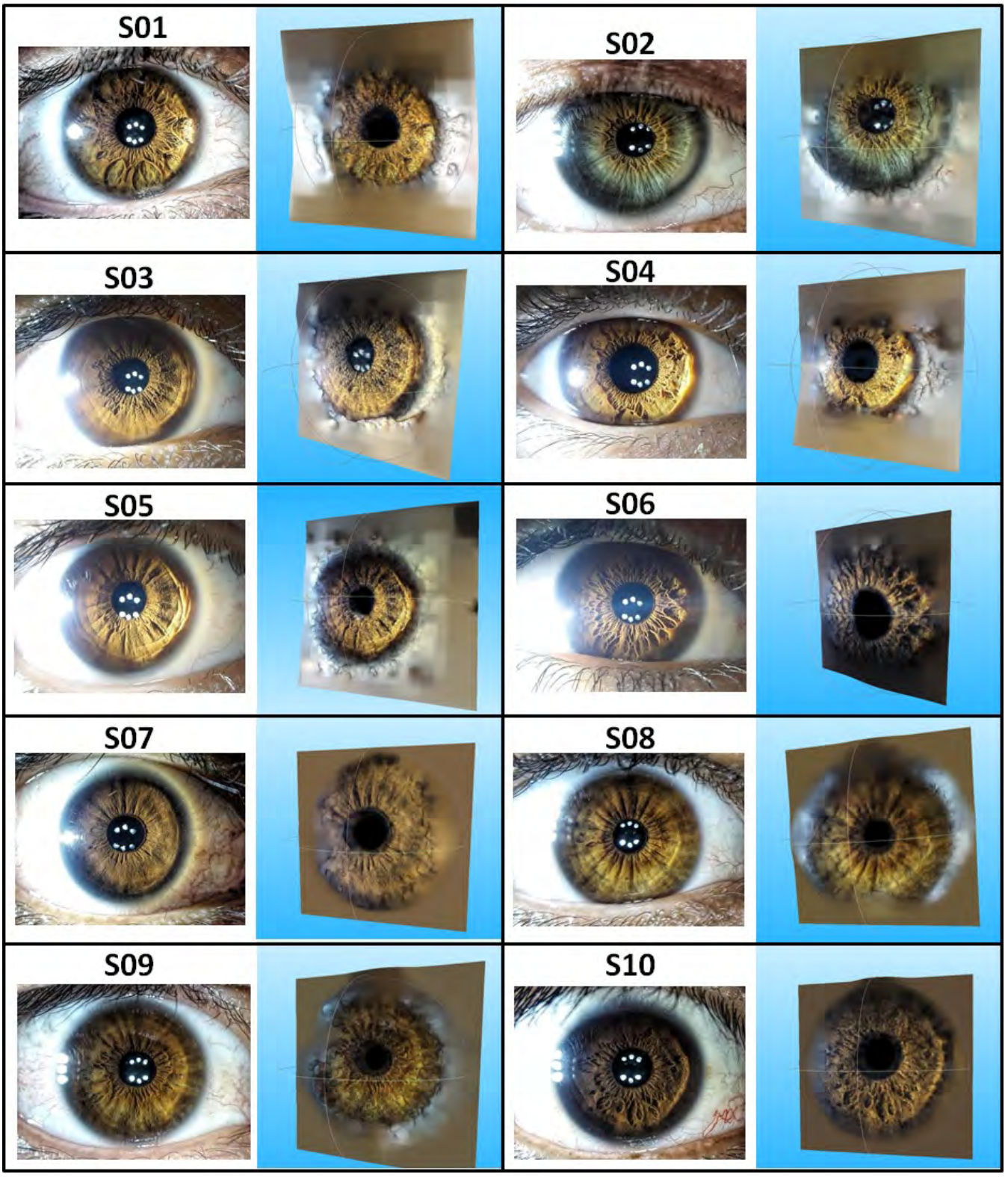

FIGURE 10. Reconstructed 3D iris models for the 10 subjects. The 3D reconstructed mesh is presented next to one of the iris images from which the model was generated. Images were captured using lateral + frontal VL.

camera motion with a linear actuator. Additionally, an OCT scan was performed on the right eye of subject 1. In the results section, we show the reconstructed 3D model for all 10 subjects, as well as a cross-section comparison between the 3D model and the OCT scan for subject 1. To compensate for the pupil dilation differences between the OCT scan

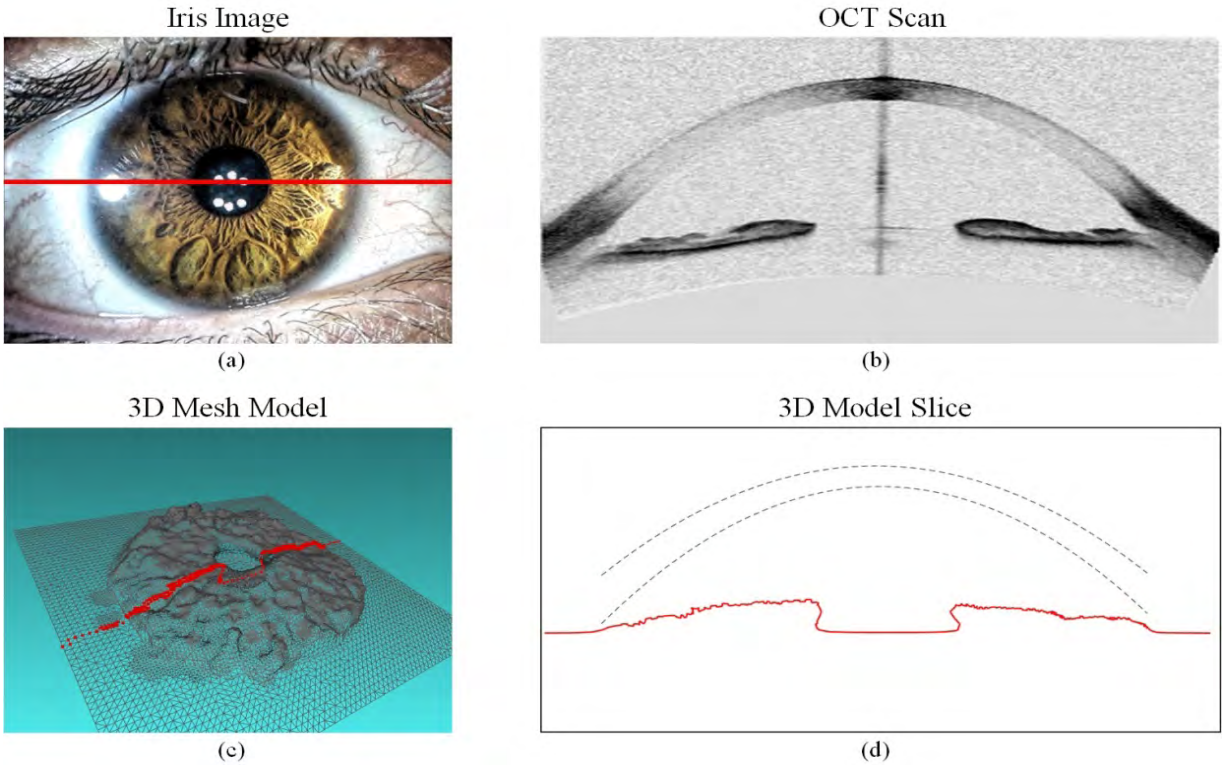

FIGURE 11. Cross-section comparison between the OCT scan and the 3D mesh model of subject 1. Red lines indicate the cutting plane. Dashed lines in (d) represent the cornea in (b). Lineal dilation was applied in (d) so that the 3D model has the same pupil dilation level as the OCT scan.

TABLE 1. Signal to noise ratio in 3D spatial patterns of known dimensions.

h [µm]	3D Points	A [µm]	σ [µm]	SNR
75	28431	79	10	7.9
150	30034	155	12	12.9
375	35023	378	12	31.5

TABLE 2. SFM methods comparison: average reconstruction error in patterns of known dimensions.

SfM Method	75 µm	150 µm	375 µm
VisualSFM / CMVS	13.3 µm	16.1 µm	12.8 µm
Regard 3D*	10.4 µm	13.7 µm	13.2 µm
Ours	7.8 µm	9.5 µm	9.2 µm

* Available online on: http://www.regard3d.org/

and the 3D model, a linear deformation was applied to the 3D model slice until both methods have the same dilation level [10].

IV. RESULTS

A. RESULTS FOR THE PROPOSED METHOD SPATIAL RESOLUTION

We scanned the three 3D patterns described in section III.F and measured the amplitude of step A, as well as the standard deviation of the noise σ. Fig. 9 shows an example of a scanned 3D pattern. The lower and upper levels of the pattern were segmented using two thresholds on the z axis. The cross-section shown in Fig. 9b is for illustrative purposes only, since the analysis was made using the 3D segmented data that is shown in Fig. 9c. Since we are interested in measuring the height of the step as the difference between the lower and upper levels, green points in Fig. 9c were not used in the analysis.

Table 1 shows the results of this test for the three spatial patterns 75 μm, 150 μm, and 375 μm. The height of each step was measured with an error smaller or equal to 5μm in all of the three samples. As expected, the SNR increases proportionally to the height of the step. The level of the noise present in our method is consistent for the three models with a value of $11\mu\text{m} \pm 1\mu\text{m}$. This implies that the smallest detail we can detect is 11μm.

Table 2 shows that our SfM algorithm produced reconstruction errors smaller than 10μm. These results are consistent with those of Table 1. Additionally, our method produced smaller errors than those of the other two SfM algorithms tested.

B. SUBJECTS' IRIS RECONSTRUCTION RESULTS

The 3D iris surfaces of 10 subjects were reconstructed using the proposed methodology. Fig. 10 shows, for each subject in one row, the frontal iris image followed by one image taken from the 3D model at a specific angle. It can be observed that the final 3D model captures the depth information, as well as detail information from the iris. In general, the regions of the iris with greater texture produced more intricate shapes in the final 3D iris reconstruction. Fig. 11c shows a close up of

TABLE 3. Reconstructed 3D-model summary.

Subject	3D Points	Polygons	PP [mm]	STD[mm]
S01	12,006	66,273	1.53	0.31
S02	9,430	53,261	1.27	0.25
S03	13,332	76,902	1.09	0.22
S04	9,683	51,146	1.21	0.24
S05	12,919	73,478	1.47	0.29
S06	6,840	31,938	1.47	0.29
S07	14,030	42,558	1.43	0.24
S08	9,934	22,376	1.38	0.24
S09	12,726	71,506	1.53	0.27
S10	10,147	56,611	1.46	0.30
Average:	**11,105**	**54,605**	**1.38**	**0.27**

model S01 from a lateral perspective. It illustrates the relief of the iris, which is captured by our method. Table 3 shows information about the reconstructed 3D models. The average peak-to-peak depth value among the models is 1.38mm, considering only the iris region. The variability of the depth value is characterized by the standard deviation. Its average value is 270μm including all the models. Finally, the average number of reconstructed 3D points is 11,105, and the average number of polygons in the 3D mesh is 54,605. The results of the cross section comparison between the 3D model and the OCT are presented in Fig. 11. The result of the OCT scan in Fig. 11b shows, as expected, the presence of non-planar relief in the surface of the iris of subject 1. Fig. 11d shows the slice of the 3D model.

V. CONCLUSIONS

We presented a new method for building a 3D model of the iris surface from several 2D iris images. Our method uses 2D VL images of the iris from different perspectives, and a modified SfM algorithm to reconstruct a 3D mesh representation of the iris. The use of a combination of lateral and frontal VL illumination is a key element in the image acquisition process, as it enhances the visibility of the structures on the iris for both dark and light colored eyes [14]. Since several 2D images from different views are acquired to build the 3D model, illuminating both eyes with the same amount of light helps maintain stable dilation. However, small dilation variation between images still occurs. To further reduce dilation related problems, an image selection process was performed identifying a set of images with very similar dilation for generating a 3D model. As a result, the number of 3D points, the shape of the reconstructed irises, and the robustness of the method improved relative to our previous research [13].

The spatial resolution of the proposed method was measured using three 3D patterns of known dimensions (75 μm, 150 μm, and 375 μm). The level of the noise present in our method is consistent for the three models with a value of 11μm $\pm$ 1μm. This implies that the smallest detail we can detect is 11μm, which means that we can measure details six times smaller than current 3D common-object scanners [48]. The resolution of our proposed method is similar to that of conventional OCT scanners, which operate in the neighborhood of 10μm [49]. However, modern OCT scanners can reach resolutions as fine as 2.2μm [50]. To put those numbers in context, the thickness of the iris tissue is about 400μm [51], [52].

We reconstructed the 3D iris models for 10 subjects, and it was observed that the final 3D model captures the depth information, as well as detail information, from the iris. We also compared an OCT for one iris to the respective crosscut performed over the 3D model of the iris. Similar spatial features were identified with both methods. To increase the precision in depth measurement, camera resolution can be improved. This would increase the number of keypoints that are used to create the 3D model and enhance the resolution.

The proposed methodology has the potential of being applied in biometrics and in ophthalmology. With the additional depth information extracted by our method, a possible line of research is to develop methods that make use of 3D data in iris recognition. This may be of special interest when only segments of the iris are available because they would contain more information than 2D segments.

Additionally, our proposed method could be useful for detecting contact lenses, and therefore is another possible area of research in iris recognition [53]–[55]. The 3D model of a colored contact lens will have a spherical shape, since the dominant texture is printed in the surface of the contact lens.

This method could also potentially be applied in the diagnosis of acute angle glaucoma [13], [14]. A current tool to diagnose this disease is Optical Coherence Tomography (OCT) [15]. OCT forms an image of a transversal cut of the eye. Ophthalmologists measure various parameters such as: the width of the iris, the angle between the iris and the cornea, and the distance between the anterior chamber and the top of the iris, for the diagnosis [15].

A 3D mesh representation of the iris can also be used as a tool for studying pupil dilation in greater detail. The deformation of the iris tissue due to pupil dilation typically treated as linear although it is known that this is only an approximation [5], [10]. This motivated research into more accurate iris normalization models that improve iris recognition performance under dilation differences [12], [56]–[58]. For instance, Clark et al. generated a non-linear iris normalization model based on the biomechanical proprieties of the iris [12]. Studying this phenomenon in 3D with real irises could produce valuable insights, and it might lead to the formulation of a more accurate iris normalization model.

A limitation of our method is the specular reflection of the lateral LED. Due to the saturation of this light, a segment of the iris is lost in the reconstruction. A possible solution to this problem is to place an additional lateral LED on the other side of the eye, and capture two sets of images that then can be combined for the 3D models.

ACKNOWLEDGMENT

The authors would also like to thank the students at the School of Engineering, Universidad de Chile, who participated enthusiastically as volunteers for iris image acquisition.

REFERENCES

[1] J. Daugman, "The importance of being random: Statistical principles of iris recognition," *Pattern Recognit.*, vol. 36, no. 2, pp. 279–291, 2003.

[2] A. K. Jain, A. Ross, and S. Prabhakar, "An introduction to biometric recognition," *IEEE Trans. Circuits Syst. Video Technol.*, vol. 14, no. 1, pp. 4–20, Jan. 2004.

[3] K. W. Bowyer, K. Hollingsworth, and P. J. Flynn, "Image understanding for iris biometrics: A survey," *Comput. Vis. Image Understand.*, vol. 110, no. 2, pp. 281–307, 2008.

[4] K. W. Bowyer and M. J. Burge, "Introduction to the handbook of iris recognition," in *Handbook of Iris Recognition*. London, U.K.: Springer, 2016, pp. 1–14.

[5] J. Daugman and I. Malhas, "Iris recognition border-crossing system in the UAE," *Int. Airport Rev.*, vol. 8, no. 2, pp. 49–53, 2004.

[6] J. Daugman, "600 million citizens of India are now enrolled with biometric ID," *Proc. SPIE Newsroom*, vol. 7, pp. 1–4, May 2014.

[7] K. W. Bowyer, E. Ortiz, and A. Sgroi, "Trial Somaliland voting register de-duplication using iris recognition," in *Proc. 11th IEEE Int. Conf. Workshops Autom. Face Gesture Recognit.*, vol. 2, May 2015, pp. 1–8.

[8] J. Daugman, "How iris recognition works," *IEEE Trans. Circuits Syst. Video Technol.*, vol. 14, no. 1, pp. 21–30, Jan. 2004.

[9] J. Daugman and C. Downing, "Epigenetic randomness, complexity and singularity of human iris patterns," *Proc. Roy. Soc. B, Biol. Sci.*, vol. 268, no. 1477, pp. 1737–1740, 2001.

[10] K. Hollingsworth, K. W. Bowyer, and P. J. Flynn, "Pupil dilation degrades iris biometric performance," *Comput. Vis. Image Understand.*, vol. 113, no. 1, pp. 150–157, 2009.

[11] E. Celik and M. Karakaya, "Pupil dilation at synthetic off-angle iris images," in *Proc. Int. Conf. Biometrics Special Interest Group (BIOSIG)*, Sep. 2016, pp. 1–5.

[12] A. Clark, S. Kulp, I. Herron, and A. A. Ross, *A Theoretical Model For Describing Iris Dynamics*. London, U.K.: Springer, 2016, pp. 417–438.

[13] D. Bastias, C. A. Perez, D. P. Benalcazar, and K. W. Bowyer, "A method for 3D iris reconstruction from multiple 2D near-infrared images," in *Proc. IEEE Int. Joint Conf. Biometrics (IJCB)*, Oct. 2017, pp. 503–509.

[14] D. Benalcazar, C. Perez, D. Bastias, and K. Bowyer, "Iris recognition: Comparing visible-light lateral and frontal illumination to NIR frontal illumination," in *Proc. IEEE Winter Conf. Appl. Comput. Vis. (WACV)*, Jan. 2019, pp. 867–876.

[15] I. I. Bussel, G. Wollstein, and J. S. Schuman, "OCT for glaucoma diagnosis, screening and detection of glaucoma progression," *Brit. J. Ophthalmol.*, vol. 98, pp. ii15–ii19, Jul. 2014.

[16] C. Wu, "Towards linear-time incremental structure from motion," in *Proc. Int. Conf. 3D Vis.*, Jun./Jul. 2013, pp. 127–134.

[17] M. Kazhdan and H. Hoppe, "Screened poisson surface reconstruction," *ACM Trans. Graph.*, vol. 32, no. 3, pp. 1–13, 2013.

[18] Z. Zhang, "A flexible new technique for camera calibration," *IEEE Trans. Pattern Anal. Mach. Intell.*, vol. 22, no. 11, pp. 1330–1334, Nov. 2000.

[19] D. Scaramuzza, A. Martinelli, and R. Siegwart, "A toolbox for easily calibrating omnidirectional cameras," in *Proc. IEEE/RSJ Int. Conf. Intell. Robots Syst.*, Oct. 2006, pp. 5695–5701.

[20] S. Paris, S. W. Hasinoff, and J. Kautz, "Local Laplacian filters: Edge-aware image processing with a laplacian pyramid," *ACM Trans. Graph.*, vol. 58, no. 3, pp. 81–91, 2011.

[21] Y. Furukawa and C. Hernandez, "Multi-view stereo: A tutorial," *Found. Trends Comput. Graph. Vis.*, vol. 9, nos. 1–2, pp. 1–148, 2013.

[22] S. Agarwal *et al.*, "Building Rome in a day," *Commun. ACM*, vol. 54, no. 10, pp. 105–112, Oct. 2011.

[23] A. J. Davison, I. D. Reid, N. D. Molton, and O. Stasse, "MonoSLAM: Real-time single camera SLAM," *IEEE Trans. Pattern Anal. Mach. Intell.*, vol. 29, no. 6, pp. 1052–1067, Jun. 2007.

[24] R. Mur-Artal, J. M. M. Montiel, and J. D. Tardós, "ORB-SLAM: A versatile and accurate monocular SLAM system," *IEEE Trans. Robot.*, vol. 31, no. 5, pp. 1147–1163, Oct. 2015.

[25] P. Corke, *Robotics, Vision and Control: Fundamental Algorithms in MATLAB*, 2nd ed. Berlin Germany: Springer 2013.

[26] G. Silveira, E. Malis, and P. Rives, "An efficient direct approach to visual SLAM," *IEEE Trans. Robot.*, vol. 24, no. 5, pp. 969–979, Oct. 2008.

[27] Y. Furukawa and J. Ponce, "Accurate, dense, and robust multiview stereopsis," *IEEE Trans. Pattern Anal. Mach. Intell.*, vol. 32, no. 8, pp. 1362–1376, Aug. 2008.

[28] W. Fang, Y. Zhang, B. Yu, and S. Liu, "FPGA-based ORB feature extraction for real-time visual SLAM," in *Proc. Int. Conf. Field Program. Technol. (ICFPT)*, Dec. 2017, pp. 275–278.

[29] A. Pumarola, A. Vakhitov, A. Agudo, A. Sanfeliu, and F. Moreno-Noguer, "PL-SLAM: Real-time monocular visual SLAM with points and lines," in *Proc. IEEE Int. Conf. Robot. Automat. (ICRA)*, May/Jun. 2017, pp. 4503–4508.

[30] R. Egodagamage and M. Tuceryan, "A collaborative augmented reality framework based on distributed visual Slam," in *Proc. Int. Conf. Cyberworlds (CW)*, Sep. 2017, pp. 25–32.

[31] Y. Furukawa and J. Ponce, "Accurate camera calibration from multi-view stereo and bundle adjustment," *Int. J. Comput. Vis.*, vol. 84, no. 3, pp. 257–268, Apr. 2009.

[32] B. Triggs, P. F. McLauchlan, R. I. Hartley, and A. W. Fitzgibbon, "Bundle adjustment—A modern synthesis," in *Proc. Int. Workshop Vis. Algorithms*, 1999, pp. 298–372.

[33] N. Campbell, G. Vogiatzis, C. Hernández, and R. Cipolla, *Using Multiple Hypotheses To Improve Depth-Maps for Multi-View Stereo*. Berlin, Germany: Springer, 2008, pp. 766–779.

[34] C. Hernandez, G. Vogiatzis, and R. Cipolla, "Probabilistic visibility for multi-view stereo," in *Proc. IEEE Conf. Comput. Vis. Pattern Recognit.*, Jun. 2007, pp. 1–8.

[35] C. H. Esteban and F. Schmitt, "Silhouette and stereo fusion for 3D object modeling," *Comput. Vis. Image Understand.*, vol. 96, no. 3, pp. 367–392, 2004.

[36] J. Mélou, Y. Quéau, J.-D. Durou, F. Castan, and D. Cremers, *Beyond Multi-View Stereo: Shading-Reflectance Decomposition*. Cham, Switzerland: Springer, 2017, pp. 694–705.

[37] J. Z. Lim, H. Suzuki, S. Utsugi, and H. Katai, "Experimental development of a multi-view stereo endoscope system," in *Proc. 2nd Russia Pacific Conf. Comput. Technol. Appl. (RPC)*, Sep. 2017, pp. 14–18.

[38] M. Alex, M. A. Banks, L. Phillipi, L. Yu, J. Taylor, and S. N. Patel, "Biliscreen: Smartphone-based scleral jaundice monitoring for liver and pancreatic disorders," *Proc. ACM on Interact. Mobile, Wearable Ubiquitous Technol.*, vol. 1, no. 26, p. 20, 2017.

[39] Google. *Google Cardboard Google VR*. Accessed: Sep, 13, 2018. [Online]. Available: https://vr.google.com/cardboard/

[40] The MathWorks, *Single Camera Calibrator App MATLAB Simulink*. Accessed: Sep, 12, 2018. [Online]. Available: https://la.mathworks.com/help/vision/ug/single-camera-calibrator-app.html

[41] L. Masek, "Recognition of human iris patterns for biometric identification," M.S. thesis, Univ. Western Australia, Perth, WA, Australia, 2003.

[42] P. Loncomilla, J. Ruiz-Del-Solar, and L. Martínez, "Object recognition using local invariant features for robotic applications: A survey," *Pattern Recognit.*, vol. 60, pp. 499–514, Dec. 2016.

[43] H. Bay, A. Ess, T. Tuytelaars, and L. Van Gool, "Speeded-up robust features (SURF)," *Comput. Vis. Image Understand.*, vol. 110, no. 3, pp. 346–359, 2008.

[44] B. Horn. (Jun. 4, 2014). *Recovering Baseline and Orientation from Essential Matrix*. [Online]. Available: http://ocw.mit.edu/courses/

[45] M. A. Fischler and R. C. Bolles, "Random sample consensus: A paradigm for model fitting with," *Commun. ACM*, vol. 24, pp. 381–395, Jun. 1981.

[46] J. Shi and C. Tomasi, *Good Features to Track*. Ithaca, NY, USA: Cornell Univ. 1993.

[47] P. Cignoni, M. Callieri, M. Corsini, M. Dellepiane, F. Ganovelli, and G. Ranzuglia, "MeshLab: An open-source mesh processing tool," in *Proc. Eurograph. Italian Chapter Conf.*, 2008, pp. 129–136.

[48] M. Lansard. (2018). The 10 Best 3D Scanners in 2018 Reviews and Buying Guide. ANIWAA. Accessed: Jan. 22, 2019. [Online]. Available: https://www.aniwaa.com/best-3d-scanner/

[49] A. Fouad *et al.*, "Variations in optical coherence tomography resolution and uniformity: A multi-system performance comparison," *Biomed. Opt. Express*, vol. 5, no. 7, pp. 2066–2081, Jul. 2014.

[50] Thorlabs. (2019). OCT Selection Guide. Thorlabs, Inc. Accessed: Jan. 22, 2019. [Online]. Available: https://www.thorlabs.com.

[51] A. Invernizzi, M. Cigada, L. Savoldi, S. Cavuto, L. Fontana, and L. Cimino, "*In Vivo* analysis of the iris thickness by spectral domain optical coherence tomography," *Brit. J. Ophthalmol.*, vol. 98, no. 9, pp. 1245–1249, Sep. 2014.

[52] M. He, D. Wang, J. W. Console, J. Zhang, Y. Zheng, and W. Huang, "Distribution and heritability of iris thickness and pupil size in chinese: The guangzhou twin eye study," *Investigative Ophthalmol. Vis. Sci.*, vol. 50, no. 4, pp. 1593–1597, Apr. 2009.

[53] Z. He, Z. Sun, T. Tan, and Z. Wei, *Efficient Iris Spoof Detection Via Boosted Local Binary Patterns*. Berlin, Germany: Springer, 2009, pp. 1080–1090.

[54] K. Hughes and K. W. Bowyer, "Detection of contact-lens-based iris biometric spoofs using stereo imaging," in *Proc. 46th Hawaii Int. Conf. Syst. Sci.*, Jan. 2013, pp. 1763–1772.
[55] A. Czajka, Z. Fang, and K. Bowyer, "Iris presentation attack detection based on photometric stereo features," in *Proc. IEEE Winter Conf. Appl. Comput. Vis. (WACV)*, Jan. 2019, pp. 877–885.
[56] I. Tomeo-Reyes, A. Ross, A. D. Clark, and V. Chandran, "A biomechanical approach to iris normalization," in *Proc. Int. Conf. Biometrics (ICB)*, 2015, pp. 9–16.
[57] S. Shah and A. Ross, "Iris segmentation using geodesic active contours," *IEEE Trans. Inf. Forensics Security*, vol. 4, no. 4, pp. 824–836, Dec. 2009.
[58] M. Vatsa, R. Singh, and A. Noore, "Improving iris recognition performance using segmentation, quality enhancement, match score fusion, and indexing," *IEEE Trans. Syst. Man, Cybern. B, Cybern.*, vol. 38, no. 4, pp. 1021–1035, 2008.

DANIEL P. BENALCAZAR (M'09) was born in Quito, Ecuador, in 1987. He graduated in electronics and control engineering from the Escuela Politecnica Nacional, Quito, in 2012. He received the master's degree in electrical engineering from The University of Queensland, Brisbane, Australia, in 2014, with a minor in biomedical engineering. He is currently pursuing the Ph.D. degree with the Universidad de Chile, Santiago, Chile. From 2015 to 2016, he was a Professor with the Central University of Ecuador. Ever since, he has participated in various research projects in biomedical engineering and biometrics.

DIEGO BASTIAS received the B.S. degree in electrical engineering and the P.E. title (Hons) in electrical engineering from the Universidad de Chile, in 2014 and 2016, respectively, where he is currently with the Department of Electrical Engineering as a Research Assistant. His current research interests include biometrics and computer vision.

CLAUDIO A. PEREZ received the B.S. and P.E. degrees in electrical engineering and the M.S. degree in biomedical engineering from the Universidad de Chile, in 1980 and 1985, respectively, and the Ph.D. degree from The Ohio State University, in 1991. He was a Fulbright Student with The Ohio State University, where he obtained a Presidential Fellowship, in 1990. He was a Visiting Scholar with UC Berkeley, in 2002, through the Alumni Initiatives Award Program from the Fulbright Foundation. He was the Department Chairman, from 2003 to 2006, and the Director of the Office of Academic and Research Affairs, School of Engineering, Universidad de Chile, from 2014 to 2018. He is currently a Professor with the Department of Electrical Engineering, Universidad de Chile. His research interests include biometrics, image processing applications, and pattern recognition. He is a Senior Member of the IEEE and the Systems, Man and Cybernetics and IEEE-CIS Societies.

KEVIN W. BOWYER is currently the Schubmehl-Prein Family Professor with the Department of Computer Science and Engineering, University of Notre Dame, and also serves as the Director of the College of Engineering Summer International Programs. His main research interests include computer vision and pattern recognition, including biometrics, data mining, object recognition, and medical image analysis. He is a Fellow of the IEEE for his contributions to algorithms for recognizing objects in images and a Fellow of the IAPR for his contributions to computer vision, pattern recognition, and biometrics. He received the IEEE Computer Society Technical Achievement Award for pioneering contributions to the science and engineering of biometrics and the inaugural IEEE Biometrics Council Meritorious Service Award. He is serving as the inaugural Editor-In-Chief for the IEEE TRANSACTIONS ON BIOMETRICS, BEHAVIOR, AND IDENTITY SCIENCE (T-BIOM).